CMOS image sensors for X-ray interferometry

T. W. Buggey[a], M. W. J. Hubbard[a], K. Stefanov[a] , A. D. Holland[a], and D. J. Hall[a]

[a]Centre for Electronic Imaging (CEI), The Open University, Milton Keynes, United Kingdom, MK7 6AA

ABSTRACT

X-ray interferometry (XRI) was first demonstrated in the early 2000's, and many early mission concepts followed which exploited the significant improvement in spatial resolution that XRI offered. Unfortunately, optical technology was not mature enough to meet the requirements, and the idea remained dormant. ESA's voyage 2050 programme, in combination with optical and pointing accuracy technology developments, has reignited interest in the concept, but large technological challenges still remain to realise such a groundbreaking telescope. Given the spectral and now *spatial* requirements of a XRI, the next generation of detector technologies must be developed which can meet those requirements to enable such a telescope.

For the proposed ESA THESEUS X-ray astronomy mission, strict requirements on instrument operating temperature (-40 °C) have necessitated developments of new detectors technologies, namely CMOS image sensors (CIS). The CEI, in collaboration with Te2v, have designed, manufactured, and characterised a monolithic fully depleted CIS specifically optimised for soft X-ray astronomy. The prototype detector currently meets the THESEUS soft X-ray imager requirements and boasts a near Fano-limited energy resolution of 130 eV (@5.9 keV) at -40°C. Although the new technology can perform well, the specific detector requirements of XRI need to balance opposing parameters of spatial and energy resolution. This paper will outline the current performance of the CIS221-X for soft X-ray astronomy (as well as other competing technologies) and describe future plans for developing CIS to meet the challenging requirements of XRI.

Keywords: X-ray astronomy, ESA, X-ray interferometry, CMOS image sensors, X-rays, silicon detectors

1. INTRODUCTION

The first laboratory detection of X-ray interference fringes was shown in the early 2000's [1] and a surge of activity in the form of novel missions concepts and enabling technology was conceptualised over the next decade [2,3]. Although key technology was conceptualised, manufacturing hardware was not yet possible, and the idea lay dormant until a white paper for ESA voyage 2050 recently reignited the idea [4]. Since then, work to develop key pieces of technology such as optics, pointing accuracy technology, detectors, and test facilities [4] has begun in different forms across different institutions. Both the UK Space Agency (UKSA) and the Netherlands Institute of Space Research (SRON) have funded distinct (but complementary) technology roadmaps, outlining the path to develop the technology and raise the technology readiness level (TRL) so mission concepts can be matured. Although large technological hurdles still need to be overcome, ESA are specifically interested in technology development for X-ray interferometry (XRI) due to the huge improvement in spatial resolution offered by such a telescope.

This paper will specifically focus on detector developments for a XRI, outlining the potential of recent technology developments in the form of CMOS image sensors (CIS) which were developed for ESA's THESEUS soft X-ray imager (SXI). Although CIS are now clearly viable (and operating at near Fano-limit) for spectroscopic X-ray astronomy (meeting the requirements of THESEUS' SXI), the spatial resolution

X-Ray, Optical, and Infrared Detectors for Astronomy XI, edited by Andrew D. Holland, Kyriaki Minoglou, Proc. of SPIE Vol. 13103, 131030A · © 2024 SPIE
0277-786X · doi: 10.1117/12.3018322

requirements of interference fringe imaging directly oppose the current pixel design philosophy of silicon image sensors for X-ray astronomy. MOS CCDs as part of EPIC on XMM-Newton, and now CIS for THESEUS' SXI have all found that square pixels of ~40 microns are optimal for minimal charge sharing, and hence the best spectroscopic (energy resolution) performance. Spatial resolution (absolutely necessary for XRI) of parallel interference fringes with 10 micron separation or less is not possible with detectors of this size.

This paper will provide background into the optical setup of an XRI, and how this optical setup places requirements on the detectors. An assessment of current imaging technologies will follow, which will show why specific technology developments are necessary, while also providing background into the pros and cons of silicon detectors versus alternative technologies (calorimeters). The current performance of the CIS developed for THESEUS SXI (named CIS221-X) will be summarised, and new future pixel developments, specifically a rectangular pixel variant which can meets the needs of an XRI focal plane will be presented. The rectangular pixel design aims to find a compromise between the necessary spatial resolution requirements of XRI, but also maximise energy resolution, which is also a key quantity. Due to the early nature of the work, only X-ray event simulations will be presented, with a goal to validate the X-ray event simulations on the CIS221-X 40 micron pixels, and then use that data to predict what the energy resolution of different asymmetric pixel variants will be.

2. OVERALL MISSION CONCEPT AND DETECTOR DESIGN

After the initial experimental demonstration of X-ray interference fringes, attention turned to practical applications of the concept, and how it could be exploited to vastly improve the spatial resolution of X-ray telescopes. Ideas centred around concepts for a telescope, and although the μ-arcsec performance was a significant improvement, the concept required formation flying of multiple spacecraft [5,6,7]. It was not until a novel optical concept using a slatted mirror was developed, shown in Figure 1, that the idea for a spacecraft could be simplified to a single-spacecraft solution. The optical arrangement is comprised of two collecting mirrors (M_1 and M_3) separated by distance D, known as the baseline. The two collecting mirrors focus incoming photons towards the combining mirrors (M_2 and M_4), where M_2 is the novel slatted mirror. The slatted mirror facilitates constructive interference between two incoming coherent beams of photons, producing an interference fringe pattern at a distance X from the collecting mirrors, anywhere in a volume A. For a single-spacecraft XRI, the distance D is ~2 m and the distance X is ~20 m. the distance X can be achieved within a single-spacecraft volume via a deployable mechanism.

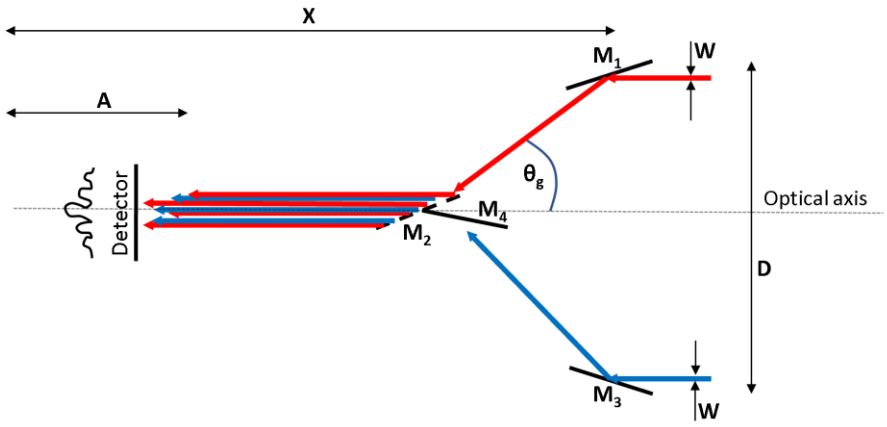

Figure 1: Schematic of the Willingale geometry for a single-spacecraft XRI, with key dimensions D and X shown. Note that some dimensions are not to scale so that all key features are clearly visible. Two separate beams of X-rays are incident from the right-hand side of the page, with trajectories through the instrument indicated by the red and blue lines. The beams of X-rays overlap, causing interference fringes across a finite volume, shown by the distance A.

The optical pattern produced by a slatted mirror arrangement is a distinct pattern of long and narrow interference fringes, with two examples shown in Figure 2. As an example, for a XRI of 1 m baseline (D), and a distance of X = 20 m, a fringe pattern is ~50 cm long, 100 micron wide, and separated by a distance of 30 microns. Therefore, unlike standard X-ray telescopes, the performance of a XRI is also a function of the spatial resolution of the imaged fringe pattern produced by the optics. Although spatial detector requirements are now also imposed by a XRI, energy resolution is still important as a lower energy resolution can significantly reduce the optical requirements. This poses problems for the current pixel design paradigm of X-ray detectors for X-ray astronomy, as large pixels (~40 microns) have been shown to be optimal for charge collection and hence energy resolution. Resolving interference fringe separation of even < 30 microns will be challenging, although rectangular pixel dimensions could be employed as the spatial resolution requirements are only in one dimension. There is a trade-off however, as rectangular pixels will suffer degraded energy resolution (and hence stricter optical requirements) due to overall lower pixel collecting area, and this is a key focus for future developments.

Along with spatial and energy resolution requirements, detector requirements also pertain other metrics such as temperature of operation, frame rates, radiation hardness, detector size, and ability to tile the detector into a suitable focal plane. Different technologies for X-ray imaging broadly fall into two fields: silicon (Si)-based approaches, and calorimeters, each with their own strengths and weaknesses. Designing a detector to meet the needs of XRI is challenging, so section 3 will summarise the current state-of-the-art of X-ray imaging technology and highlight the strengths that CIS can provide.

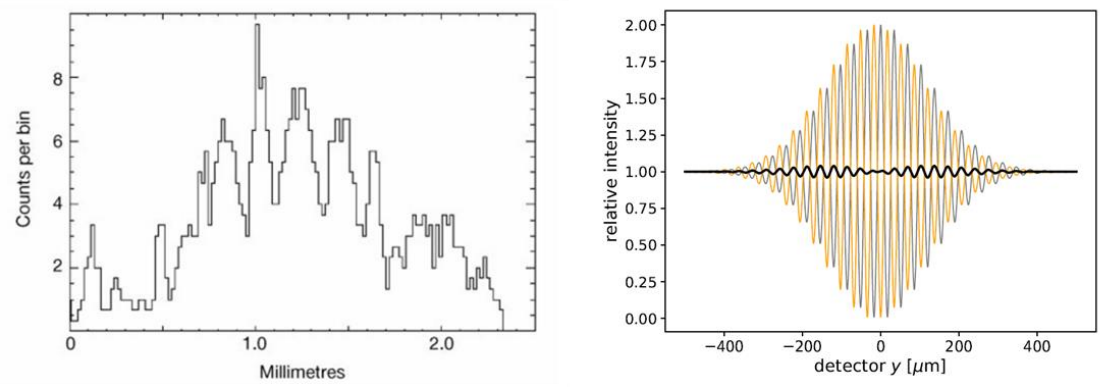

Figure 2: Example images of fringe envelopes. Left – Measured fringes in the laboratory. Right – Simulated fringe enveloped (black), from two separate X-ray sources (orange and black).

3. ASSESSMENT OF CURRENT TECHNOLOGIES

Silicon-based imaging technologies are diverse, including charge-coupled devices (CCDs), monolithic CIS, hybrid CIS, silicon drift detectors (SDDs), and DEPFET's. **Error! Reference source not found.** shows a non-exhaustive summary of the current silicon detectors for X-ray astronomy and associated missions, along with calorimeters which are being developed for the Lynx [8] telescope. For each technology, key metrics for XRI such as readout noise, pixel pitch, energy resolution, quantum efficiency, detector area, readout speed, and operating temperature are highlighted. The main difference between silicon-based technology and calorimeters is the limit of energy resolution. Silicon is limited by the Fano limit (approximately 120 eV FWHM @ 5898 eV for example), whereas calorimeters can achieve significantly lower energy resolution which makes a strong case for XRI. This comes at the expense of significantly lower temperature requirements, with silicon technology needing to be operated at temperature of between 173 K and 253 K dependent on the specific

technology, and calorimeters requiring mK temperatures. A significant amount of spacecraft resources would be required for thermal subsystems for a calorimeter-based XRI detector system.

If silicon technology is to be chosen, then it must be capable of operating at, or near, the Fano-limit. A number of pixelated technologies are currently being developed which are capable of this, including advanced CCDs [9], monolithic CIS [10-12], and DEPFETs [13]. Of these technologies, monolithic CIS have additional benefits including inherent radiation hardness [14], low power consumption, warmer operating temperatures due to the pinned photodiode, and high frame rates which can allow even warmer operational temperatures.

Table 1: Summary of current (non-exhaustive) silicon and alternative technologies for X-ray astronomy. Detector size was calculated by taking the raw number of pixels multiplied by the pixel pitch.

Detector	Read noise (e- rms)	Energy range (keV)	Pixel pitch (µm)	FWHM	QE	Detector size (cm^2)	Readout time (per frame)	Operating temperature (K)
ATHENA DEPFET [13,15]	~ 1 – 3	0.2 – 15	130 x 130	<170 eV @ 7 keV <80 eV @ 1 keV	20% @277 eV 80% @1000 eV 90% @10000 eV	0.7	80 µs – 5 ms	~190K
CCDs - CCD370 (SMILE) [16]	5	0.2 – 2	108 x 108 (6x binning)	140eV @ 5.9 keV	60% @ 200 eV 90% @ 500 eV 93% @ 1000 eV	66	~ 3 s	~150K – 170K
CCDs – MIT-LL CCDID89 [9,17]	2 - 6		16 x 16	126 – 200 eV @ 5.9 keV	N/A	12.5	~ 0.16 s	203 K
Monolithic CMOS - CIS221-X [11,12]	3.5	2 – 5	40 x 40	130eV @ 5.9 keV	73% @ 500 eV 90% @ 1000 eV 83% @ 1700 eV	4	~ 0.03 s	233K
Monolithic CMOS - GSENSE1 516BSI [18]	< 5	0.5 - 30	15 x 15	180 eV @ 5.9 keV	N/A	36	~ 0.05 s – 0.01 s	~ 243 K
Hybrid CMOS – Lynx [19]	5. 4	0.5 - 6	12.5 x 12.5	148eV @ 5.9 keV	92 % @ 1000 eV 95 % @ 4000 eV	0.0256	~ 0.01 s	150 K
SDD (Chandrayaan-2 [20,21])	~10	1 - 15	N/A	~150 eV @ 5.9 keV	N/A	0.3	~3 µs	~233K
SDD (LOFT [22-24])	~ 17	2 – 30	145 x 145	~200 eV @ 6 keV	~39% at 2 keV ~97% at 9 keV	~ 50	~ 10 µs	~233K – 263K
TES -Lynx main array [8]	N/A	0.2 – 7	50 x 50	3 – 5 eV	>80% at 6 keV	~2	0.5 µs	~65 mK
TES – Lynx enhanced array [8]	N/A	1 – 7	25 x 25	3 – 5 eV	>95% at 7 keV	~0.09	2 µs	~65 mK
TES – Lynx ultra hi-res [8]	N/A	0.2 - 0.75	50 x 50	0.3- 2eV	>99% at 0.75 keV	~0.09	0.3 µs	~65 mK

The CIS221-X device (Figure 3) has been developed specifically for the soft X-ray imager (SXI) on the THESEUS telescope by the Centre for Electronic Imaging (CEI), in collaboration with Te2v in the UK. The

Fano-limited resolution is enabled by the patented deep-depletion extension (DDE) implant, which allows full depletion via reverse biasing of the sensor. The first phase of work developed the test device, with multiple pixel variants in a single device, with one pixel variant showing world-leading energy resolution for a CIS (performance summary in **Table 2**). The next phase of work – starting mid/late 2024 will take this pixel variant, and utilise Te2v's next-generation CIS detector platform – the CIS300, to create a CIS that can meet the area requirements of the SXI focal plane. A 4.5 x 9 cm device will be manufactured by Te2v, and characterised by the CEI, which will significantly improve the chances of a successful mission adoption of THESUES at ESA's M7 candidate selection. With the new CIS300 readout architecture, lower readout noise process will be available (approx. 1.5 e^- rms), along with readout speeds of up to 240 frames per second. These two improvements will enable an even better energy resolution through decreased readout noise, and even warmer operational temperatures due to dark signal-suppressing high framerates.

Although the developments of monolithic CIS for THESEUS SXI have been rapid and show great promise in certain areas (energy resolution, detector area, framerates), the pixel geometry is still tailored only to spectral performance. As mentioned in section 2, XRI also has spatial resolution requirements for interference fringe imaging/resolution, and a 40 micron square pixel will not be sufficient. Therefore, to meet the needs of XRI, a rectangular pixel variant of the CIS221-X will be manufactured and characterised. Pixel variants in this new detector will qualitatively be able to meet the 1-dimensional spatial needs of XRI (approx. 10 micron or less), and exact pixel geometries will be of the order 10 × 50 micron. Clearly, a 10 × 50 micron pixel will suffer degraded energy resolution compared to the 40 micron square variant, the exact quantity of which is currently unknown. To understand the effect of charge spreading (and hence energy resolution) on asymmetrical pixel pitch, preliminary detector simulations can be used to help understand more explicitly the trade-off in energy resolution, but also to help inform exact dimensions of the future test pixels.

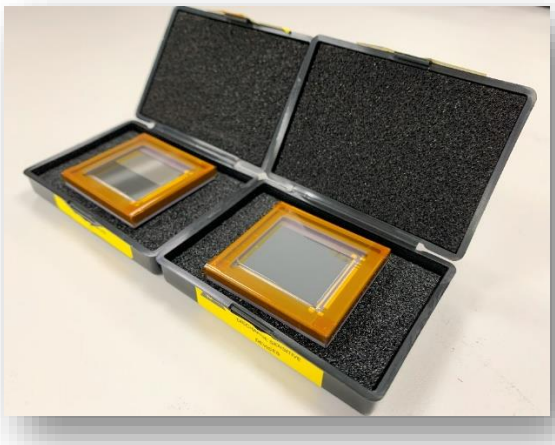

Figure 3: CIS221-X CIS designed for the THESEUS SXI. Left – A device with 50% optical blocking filter covering OBF). Right – A device with 0% OBF coating.

Table 2: CIS221-X parameter and electro-optical performance summary.

Parameter name	Value
Pixel pitch	40 µm × 40 µm
Sensor area	2 cm × 2 cm
Depletion depth	35 µm
OBF coating	Yes (50%)
Readout noise (e^- rms)	3
Dark current (e^-/pixel/sec @ -40 °C)	25
Energy resolution (@ 5898 eV)	130
Image lag (@ 10 ke^-)	< 0.1 %

4. PRELIMINARY DETECTOR SIMULATIONS

Simulated X-ray events were generated using a bespoke pipeline. The steps of the simulation pipeline are outlined below:

1. Randomised point-source locations across a 2D array are generated for a given number of X-ray events
2. Each X-ray event is assigned an energy according to an Fe-55 energy spectrum distribution
3. The interaction depth for each photon is calculated using the Beer-Lambert law
4. The number of photo-electrons generated per photon interaction is calculated based upon the ionisation energy of silicon
5. Based on a previously used and validated [25, 26] charge spread model [27], the electrons generated by each X-ray photon are assigned to a pixel based upon interactions and subsequent charge spreading in either the field-free or depleted region
6. Readout noise is then added per pixel, in addition to an electric offset
7. An image containing the simulated X-ray events is output

For this preliminary work, images containing X-ray events from a sampled Fe-55 distribution are simulated. The simulated sensor is backside-illuminated, 35 µm thick, with a square pixel pitch of 40 µm – mimicking the CIS221-X. Varying depletion depths are simulated, to investigate the effect of charge diffusion/spreading in either the field free of depleted region. For the CIS221-X, full depletion is achieved via reverse bias, and simulations show that a reverse bias of -15 V achieves full depletion. However, to ensure over-depletion, and hence maximal energy resolution, the sensor is operated using a reverse bias of -20 V. For the simulation work presented here, depletion depths of between 5 µm and 35 µm are simulated, with Figure 4 showing example X-ray images with 5 µm, 10 µm, 25 µm, and 30 µm depletion depths. For shallow depletion depths (5 µm - 10 µm), a higher proportion of X-ray events interact within the field-free zone, and photo-generated electrons drift to adjacent pixels, which is observed in both the 5 µm and 10 µm case. For the 25 µm and 30 µm depletion depth simulations (Figure 4 bottom), significantly less charge spreading is seen across all X-ray events, as the majority of events are now interacting in the depletion region where an electric field exists, facilitating efficient charge collection within the incident pixel.

After each X-ray image was simulated with varying depletion depths, each image was passed through an X-ray event detection algorithm, which selected pixels with distinct X-ray events based on a set of criteria. The criteria for X-ray event selection is shown below:

1. The noise was calculated by fitting a gaussian to the noise peak of each image. The threshold for event selection was set as 5σ above the measured noise

2. Once a pixel value is above the noise threshold, if that pixel is the maximum signal value in the 3x3 grid surrounding the incident pixel, then that pixel value and 3x3 grid is classisfied as an X-ray event

Figure 5 shows the average X-ray event profile for each depletion depth, with the 5 µm and 10 µm depletion depths showing the most charge spreading as expected. The average amount of charge spread is also similar between the two cases, as the device is still mainly undepleted, and the majority of X-rays interact in the field-free region, and are thus significantly affected by diffusion to adjacent pixels. At a depletion depth of 30 µm, the majority of electrons from each X-ray event are now in the central pixel, as most interactions are occurring in the depleted regions, and electrons are efficiently collected within a single pixel by the local electric field.

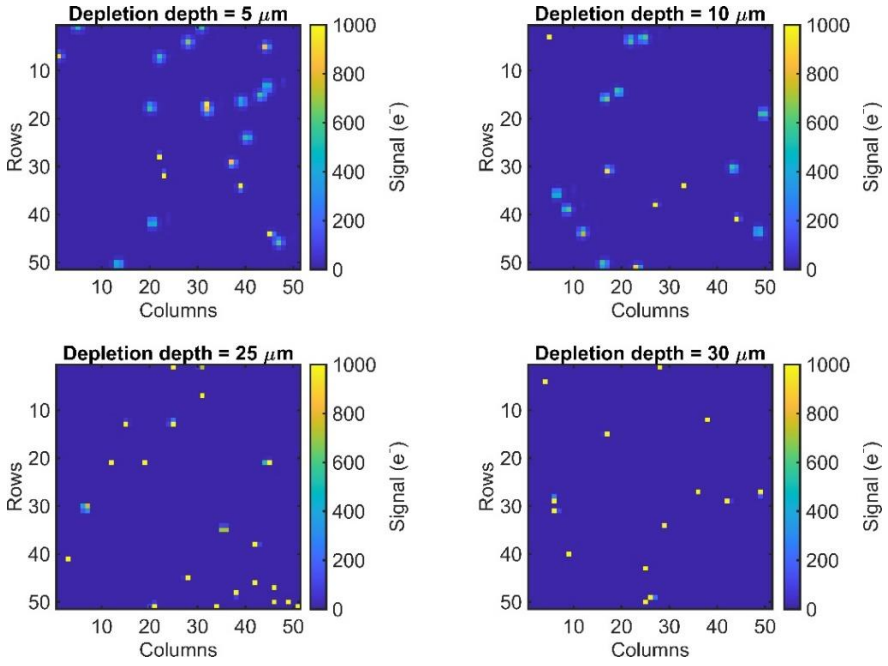

Figure 4: Example X-ray images from four separate simulations of Fe-55 events at depletion depths of 5 µm, 10 µm, 25 µm, and 30 µm.

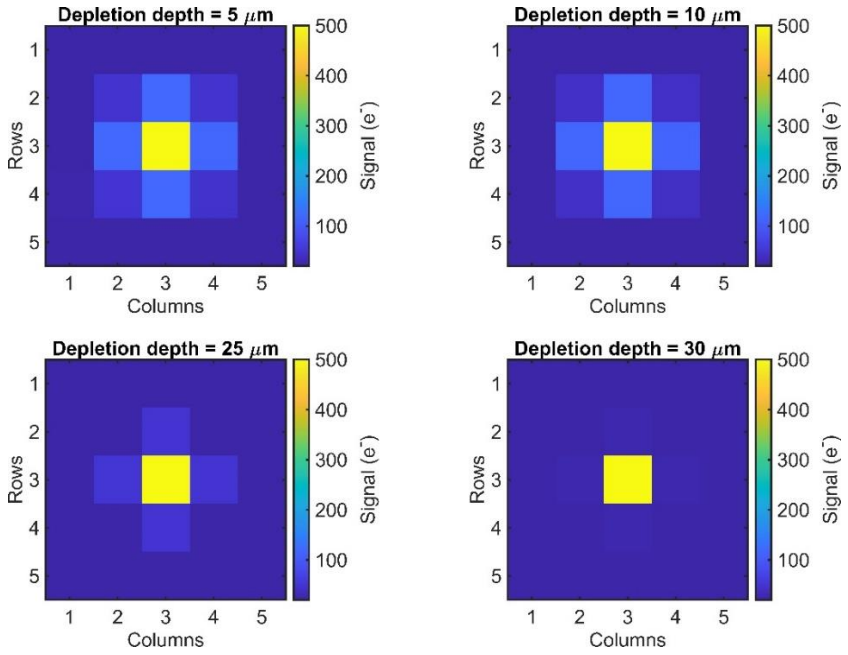

Figure 5: Average X-ray event profile of all X-ray events from the simulated Fe-55 spectrum are four different depletion depths

5. CONCLUSIONS AND FUTURE WORK

To realise a XRI, significant technology developments must be made within the fields of optics, pointing accuracy/stability hardware, test facilities, and detectors. This paper has summarised the current state of detector developments for X-ray astronomy, and shown that CIS have potential for XRI given subsequent developments (rectangular pixel variants) to meet the spatial requirements of a XRI focal plane. CIS-based solutions have added benefits over cryogenic solutions such as calorimeters, and to a lesser extent other silicon-based detectors, in the form of higher operating temperatures, inherent radiation hardness, and high frame rates. Parallel developments of CIS for the THESEUS SXI will further mature the technology, which is also absolutely necessary for XRI, in the form of optical blocking filter maturity, detector size (4.5 × 9 cm CIS for THESEUS SXI), and capabilities to tile the detector to form a large focal plane array. Furthermore, due to Teledyne e2v's recent developments of manufacturing large-format monolithic CMOS technology, device stitching capabilities could allow a highly asymmetrical detector of ~ 1.5 cm × 9 cm to be manufactured. Such a detector would be highly suited to the spatial requirements needs of XRI, and significantly boost the TRL towards a potential mission.

6. REFERENCES

[1] W. Cash, A. Shipley, S. Osterman, and M. Joy, "Laboratory detection of X-ray fringes with a grazing-incidence interferometer," *Nature*, vol. 407, no. 6801, pp. 160–162, Sep. 2000, doi: 10.1038/35025009.

[2] R. Willingale, "A practical system for x-ray interferometry," presented at the SPIE Astronomical Telescopes + Instrumentation, G. Hasinger and M. J. L. Turner, Eds., USA, Oct. 2004, p. 581. doi: 10.1117/12.552917.

[3] R. Willingale, G. I. Butcher, M. Ackermann, R. Guenther, and M. Collon, "A slatted mirror for an x-ray interferometer manufactured in silicon," presented at the SPIE Optical Engineering + Applications, S. L. O'Dell and G. Pareschi, Eds., San Diego, California, United States, Sep. 2013, p. 88611S. doi: 10.1117/12.2026534.

[4] P. Uttley *et al.*, “An x-ray interferometry concept for ESA’s Voyage 2050 programme,” in *Space Telescopes and Instrumentation 2020: Ultraviolet to Gamma Ray*, J.-W. A. den Herder, K. Nakazawa, and S. Nikzad, Eds., Online Only, United States: SPIE, Dec. 2020, p. 153. doi: 10.1117/12.2562523.
[5] K. C. Gendreau, N. White, S. Owens, W. Cash, A. Shipley, and M. Joy, “The MAXIM X-ray interferometry mission concept study,” vol. 36, pp. 11–16, Jan. 2001.
[6] K. C. Gendreau, W. C. Cash, A. F. Shipley, and N. White, “MAXIM Pathfinder x-ray interferometry mission,” presented at the Astronomical Telescopes and Instrumentation, J. E. Truemper and H. D. Tananbaum, Eds., Waikoloa, Hawai’i, United States, Mar. 2003, p. 353. doi: 10.1117/12.461316.
[7] K. C. Gendreau, W. C. Cash, A. F. Shipley, and N. E. White, “MAXIM x-ray interferometry mission,” presented at the Optical Science and Technology, SPIE’s 48th Annual Meeting, O. Citterio and S. L. O’Dell, Eds., San Diego, California, USA, Jan. 2004, p. 420. doi: 10.1117/12.506198.
[8] S. R. Bandler *et al.*, “Lynx x-ray microcalorimeter,” *J. Astron. Telesc. Instrum. Syst.*, vol. 5, no. 02, p. 1, May 2019, doi: 10.1117/1.JATIS.5.2.021017.
[9] M. W. Bautz *et al.*, “Performance of high frame-rate x-ray CCDs for future strategic missions,” in *Space Telescopes and Instrumentation 2022: Ultraviolet to Gamma Ray*, J.-W. A. Den Herder, K. Nakazawa, and S. Nikzad, Eds., Montréal, Canada: SPIE, Aug. 2022, p. 85. doi: 10.1117/12.2630139.
[10] J. Heymes *et al.*, “Characterisation of a soft X-ray optimised CMOS Image Sensor,” *J. Inst.*, vol. 17, no. 05, p. P05003, May 2022, doi: 10.1088/1748-0221/17/05/P05003.
[11] K. D. Stefanov *et al.*, “A CMOS image sensor for soft x-ray astronomy,” in *X-Ray, Optical, and Infrared Detectors for Astronomy X*, A. D. Holland and J. Beletic, Eds., Montréal, Canada: SPIE, Aug. 2022, p. 22. doi: 10.1117/12.2630733.
[12] C. Townsend-Rose *et al.*, “Electro-optical characterization of a CMOS image sensor optimized for soft x-ray astronomy,” *J. Astron. Telesc. Instrum. Syst.*, vol. 9, no. 04, Oct. 2023, doi: 10.1117/1.JATIS.9.4.046001.
[13] N. Meidinger *et al.*, “The wide field imager instrument for Athena,” presented at the SPIE Astronomical Telescopes + Instrumentation, J.-W. A. den Herder, T. Takahashi, and M. Bautz, Eds., Edinburgh, United Kingdom, Jul. 2016, p. 99052A. doi: 10.1117/12.2231604.
[14] C. Townsend-Rose, T. Buggey, J. Ivory, K. D. Stefanov, and A. D. Holland, “Ionising radiation effects in a soft X-ray CMOS image sensor,” *Nuclear Instruments and Methods in Physics Research Section A: Accelerators, Spectrometers, Detectors and Associated Equipment*, vol. 1059, p. 169011, Feb. 2024, doi: 10.1016/j.nima.2023.169011.
[15] W. Treberspurg, N. Meidinger, J. Müller-Seidlitz, and S. Herrmann, “Achievable noise performance of spectroscopic prototype DEPFET detectors,” *J. Inst.*, vol. 13, no. 12, pp. P12001–P12001, Dec. 2018, doi: 10.1088/1748-0221/13/12/P12001.
[16] S. Parsons *et al.*, “SMILE soft X-ray Imager flight model CCD370 pre-flight device characterisation,” *Earth and Planetary Physics*, vol. 8, no. 1, pp. 1–14, 2024, doi: 10.26464/epp2023057.
[17] S. Herrmann *et al.*, “X-ray speed reading: enabling fast, low noise readout for next-generation CCDs.” arXiv, Aug. 02, 2022. Accessed: May 14, 2024. [Online]. Available: http://arxiv.org/abs/2208.01247
[18] Q. Wu *et al.*, “X-Ray Performance of a Customized Large-format Scientific CMOS Detector,” *PASP*, vol. 134, no. 1033, p. 035006, Mar. 2022, doi: 10.1088/1538-3873/ac5ac9.
[19] S. V. Hull, “Hybrid CMOS detectors for the Lynx x-ray surveyor high definition x-ray imager,” *J. Astron. Telesc. Instrum. Syst.*, vol. 5, no. 02, p. 1, May 2019, doi: 10.1117/1.JATIS.5.2.021018.
[20] M. Shanmugam *et al.*, “Investigation of radiation damage due to particle irradiation on Silicon Drift Detector for Chandrayaan-2 mission,” *J. Inst.*, vol. 15, no. 01, pp. P01002–P01002, Jan. 2020, doi: 10.1088/1748-0221/15/01/P01002.
[21] M. Shanmugam, S. V. Vadawale, Y. B. Acharya, and H. S. Mazumdar, “Space radiation induced displacement damage effects on the performance of the silicon drift detector onboard chandrayaan-2 mission,” in *2015 IEEE Nuclear Science Symposium and Medical Imaging Conference (NSS/MIC)*, San Diego, CA, USA: IEEE, Oct. 2015, pp. 1–5. doi: 10.1109/NSSMIC.2015.7581891.
[22] E. D. Monte *et al.*, “The effect of the displacement damage on the Charge Collection Efficiency in Silicon Drift Detectors for the LOFT satellite,” *J. Inst.*, vol. 10, no. 05, pp. P05002–P05002, May 2015, doi: 10.1088/1748-0221/10/05/P05002.
[23] E. D. Monte *et al.*, “Measurement of the effect of non ionising energy losses on the leakage current of silicon drift detector prototypes for the LOFT satellite,” *J. Inst.*, vol. 9, no. 07, pp. P07016–P07016, Jul. 2014, doi: 10.1088/1748-0221/9/07/P07016.

[24] S. Zane, "LOFT — Large Observatory for X-ray Timing," *J. Inst.*, vol. 9, no. 12, pp. C12003–C12003, Dec. 2014, doi: 10.1088/1748-0221/9/12/C12003.
[25] M. R. Soman, "High-resolution detectors for soft X-ray spectroscopy," 2014, doi: 10.21954/OU.RO.0000A424.
[26] L. S. Jones, C. Crews, J. Ivory, and A. Holland, "A model for photon counting X-ray event reconstruction uncertainty," *J. Inst.*, vol. 19, no. 05, p. P05017, May 2024, doi: 10.1088/1748-0221/19/05/P05017.
[27] G. G. Pavlov and J. A. Nousek, "Charge diffusion in CCD X-ray detectors," *Nuclear Instruments and Methods in Physics Research Section A: Accelerators, Spectrometers, Detectors and Associated Equipment*, vol. 428, no. 2–3, pp. 348–366, Jun. 1999, doi: 10.1016/S0168-9002(99)00045-5.

7. ACKNOWLEDGEMENTS

Thank you to the UK Space Agency National Space Technology Programme for funding a technology roadmap for XRI in 2022, which has provided impetus to the UK science/technology community for developing key pieces of XRI technology. Thank you to colleagues at the University of Leicester, the Netherlands Institute for Space Research, University of Amsterdam, and the University of Colorado (Adrian Martindale, Roland den Hartog, Phil Uttley, and Webster Cash respectively) for ongoing discussions regarding the future of XRI. Finally, thank you to Matthew Soman and George Randall for their previous work on the charge spreading code which helped greatly with the simulation part of this overall work.